# Mirror symmetry decomposition in double-twisted multilayer graphene systems

Shi-Ping Ding,[1] Miao Liang,[1] Zhen Ma,[2,*] Jing-Tao Lü,[1,†] and Jin-Hua Gao[1,‡]
[1]*School of Physics and Wuhan National High Magnetic Field Center, Huazhong University of Science and Technology, Wuhan 430074, China*
[2]*School of Physics and Electronic Engineering, Zhengzhou University of Light Industry, Zhengzhou 450002, China*

(Received 29 December 2022; revised 30 July 2023; accepted 1 August 2023; published 13 November 2023)

Due to the observed superconductivity, the alternating twisted trilayer graphene (ATTLG) has drawn great research interest very recently, in which three single-layered graphene (SLG) are stacked in an alternating twist way. If one or several of the SLG in ATTLG are replaced by multilayer graphene, we get a double-twisted multilayer graphene (DTMLG). In this work, we theoretically illustrate that, if the DTMLG has a mirror symmetry along the $z$ direction like the ATTLG, there exists a mirror symmetry decomposition (MSD), by which the DTMLG can be exactly decoupled into two subsystems with opposite parity. The two subsystems are either a twisted multilayer graphene (single twist) or a multilayer graphene, depending on the stacking configuration. Such MSD can give a clear interpretation of all the novel features of the moiré band structures of DTMLG, e.g., the fourfold degenerate flat bands, and the enlarged magic angle. Meanwhile, in such DTMLG, the parity becomes a new degree of freedom of the electrons, so that we can define a parity-resolved Chern number for the moiré flat bands. More importantly, the MSD implies that all the novel correlated phases in the twisted multilayer graphene should also exist in the corresponding DTMLGs since they have the same Hamiltonian in form. Specifically, according to the MSD, we predict that the superconductivity should exist in the $(1 + 3 + 1)$-DTMLG.

DOI: 10.1103/PhysRevB.108.195119

## I. INTRODUCTION

Due to the observation of unconventional superconductivity and Mott insulating phase at the magic angle, twisted bilayer graphene (TBG) [1,2] has become the focus of research in the field of condensed matter physics in the last few years [1–4]. Although the origin of the superconductivity in TBG is still under debate, it is believed that the flat bands appearing at the magic angle will not only greatly enhance the electron correlation but also play a key role in the superconductivity of TBG [5–7]. As pointed out by further theoretical studies [8–18], the appearance of the magic angle and flat bands is a general property of the twisted multilayer graphene systems. So, an interesting question is whether we can observe superconductivity in other twisted multilayer graphene systems. The twisted double-bilayer graphene [9,13,17], and twisted monobilayer graphene (TMBG) [8,11,12] are two typical examples, which both have moiré flat bands at the magic angle. Interestingly, different from the TBG, the flat bands in the two systems are topological nontrivial [8,11–13,19], so the correlation-induced topological phenomenon can be observed in these moiré systems [9,20–22]. However, no definite signal of superconductivity has been found experimentally in both the twisted double-bilayer graphene and TMBG.

Alternating twisted trilayer graphene (ATTLG) has drawn great research interest very recently [23–50]. It is mainly because that, except the TBG [1–3,51–65], the ATTLG is the second definite moiré system, in which robust superconductivity is observed [23–27]. The ATTLG has a sandwich structure, where three single-layer graphene (SLG) are stacked in an alternating twist way with two twist angles ($\theta_{12} = -\theta_{23}$). Thus, the ATTLG has a mirror symmetry $M_z$ along the $z$ direction. An immediate consequence of the mirror symmetry is that the Hamiltonian of the ATTLG can be exactly mapped into two subsystems [29–31], namely, a TBG and an SLG, which have opposite parity (i.e., the eigenvalue of the $M_z$). Interestingly, such decomposition shows that the moiré interlayer tunneling in the TBG subsystem is scaled by a factor $\sqrt{2}$ so that the ATTLG has a larger magic angle $\sqrt{2} \times 1.05^\circ \approx 1.54^\circ$ ($1.05^\circ$ is the magic angle of the TBG) [29–31]. Meanwhile, the decomposition also clearly interprets the moiré band structure of the ATTLG near $E_f$, where one pair of moiré flat bands results from the TBG subsystem and the two linear bands are from the SLG part. It is believed that the intriguing superconductivity in ATTLG arises from the TBG subsystem of the Hamiltonian since it has the same symmetry as that of TBG [23–27].

Stimulated by the success of the ATTLG, people expect to find more moiré structures similar to the ATTLG, which can also host the superconducting phase. Very excitingly, several recent experiments report that the superconductivity will be enhanced in alternating twisted four- and five-layer graphene [66,67], which are examples of the alternating twisted multilayer graphene (AT-NLG) with $N = 4, 5$ ($N$ is the total

*mazhen@zzuli.edu.cn
†jtlu@hust.edu.cn
‡jinhua@hust.edu.cn

 

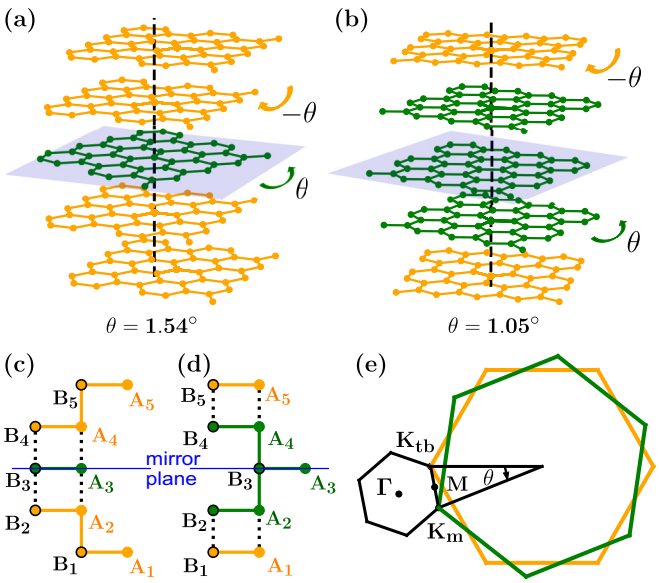


FIG. 1. Schematic diagram of the DTMLG with mirror symmetry. (a) The $(2+1+2)$-DTMLG and (b) the $(1+3+1)$-DTMGL where the twist angles $\theta$ and $-\theta$ have opposite rotation direction. (c), (d) The stacking configurations of (a) and (b), respectively. A (B) denotes the sublattice A (B) in each SLG, and the blue lines represent the mirror reflect planes. (e) The Brillouin zone of DTMLG. The subscripts of $K_m$ and $K_{tb}$ stand for the middle and top and bottom layers, respectively

number of layers). The AT-NLG means each SLG ($N \geqslant 3$) is twisted in an alternating way, i.e., the twist angles are $(\theta, -\theta, \theta, \ldots)$ [29,34,68,69]. Theoretically, it is proved that the AT-NLG can be decoupled into $\frac{N}{2}$ ($\frac{N-1}{2}$) copies of TBG if $N$ is even (odd), with an additional SLG for odd $N$ [29,34]. Note that the mirror symmetry $M_z$ also plays a key role for the AT-NLG with odd $n$.

The double-twisted multilayer graphene (DTMLG) is another kind of graphene moiré structure closely related to the ATTLG [70–73]. The DTMLG is also a sandwich structure like the ATTLG, where three van der Waals (vdW) layers are stacked in an alternating twist way with two twist angles. But, different from ATTLG, in DTMLG at least one of the three vdW layers is replaced by a multilayer graphene [70,71]. Note that we focus on the alternating twist case in this work, and do not consider the chiral twist situations [74–76]. Specifically, a general DTMLG can be denoted as an $(X+Y+Z)$-DTMLG, where $X$, $Y$, and $Z$ represent the layer number of the bottom, middle, and top vdW layers, respectively. As shown in Fig. 1, we plot the structures of two simple DTMLGs as examples, i.e., $(1+3+1)$-DTMLG and $(2+1+2)$-DTMLG. In $(1+3+1)$-DTMLG, the middle vdW layer becomes a Bernal-stacked graphene trilayer, while the top and bottom vdW layers are still SLG. Meanwhile, the $(2+1+2)$-DTMLG has bilayer graphene (BLG) as its top and bottom vdW layers, and the middle vdW layer is SLG. Very interestingly, our previous works have illustrated that the DTMLGs have fascinating moiré band structures as well [70,71]. For example, the $(1+3+1)$-DTMLG has fourfold degenerate flat bands (for the single valley and single spin), twice as much as that in TBG, at the magic angle $\theta \approx 1.05^\circ$ [71]. And the $(2+1+2)$-DTMLG has a pair of moiré flat bands at the magic angle $\theta = 1.54^\circ$, coexisting with two parabolic bands near $E_f$ [70]. Note that the DTMLG is actually a large family of moiré heterostructures since various kinds of multilayer graphene can be chosen as its vdW layers.

In this work, we consider a special kind of DTMLG, i.e., *DTMLGs with mirror symmetry* $M_z$ (see Fig. 1), where the $(1+3+1)$-DTMLG and $(2+1+2)$-DTMLG are the two simplest examples. We show that, like the ATTLG, there is also a mirror symmetry decomposition (MSD) in such kind of DTMLG, by which the DTMLG can be exactly mapped into two subsystems with opposite parity. Depending on their stacking configuration, the two subsystems are either a twisted multilayer graphene (single twist) or a multilayer graphene (no twist).

For a general $(X+Y+Z)$-DTMLG, to satisfy the mirror symmetry $M_z$, there are several apparent requirements: (1) $X = Z$, the thickness of the top and bottom vdW layers must be the same. (2) The total number of graphene layers, i.e., $X+Y+Z$, should be an odd number, which means that $Y$ has to be odd. (3) The middle vdW layer should intrinsically have mirror symmetry. The $(1+3+1)$-DTMLG is a typical example with $X = Z = 1$ and $Y = 3$, where the middle vdW layer, i.e., a Bernal-stacked (ABA-stacked) graphene trilayer, is mirror symmetric relative to the middle SLG. The middle SLG of the DTMLG here is always the reflection plane of the $M_z$ symmetry (see Fig. 1). Our study indicates that, depending on whether the middle vdW layer is SLG (i.e., $Y = 1$) or not, the MSD can be classified into two categories:

(1) When $Y = 1$, the DTMLG can be decoupled into a $(1+X)$-type twisted multilayer graphene with a magic angle $\theta = \sqrt{2} \times 1.05^\circ \approx 1.54^\circ$ (even parity) and an $X$-layer multilayer graphene (odd parity). The $(2+1+2)$-DTMLG is an example of this case.

(2) When $Y > 1$ ($Y$ need be odd in this case), the DTMLG can be decoupled into a $(X + \frac{Y+1}{2})$-type twisted multilayer graphene (even parity) and a $(X + \frac{Y-1}{2})$-type twisted multilayer graphene (odd parity). For the two subsystems, the magic angles are both $1.05^\circ$, which means there are fourfold degenerate flat bands at the magic angle. The $(1+3+1)$-DTMLG is an example of this situation.

Here, the $(1+X)$-type twisted multilayer graphene means an SLG and an $X$-layer multilayer graphene system are stacked with a twist angle (single twist). The $(X + \frac{Y\pm1}{2})$-type twisted multilayer graphene is defined in the same way, where $\frac{Y\pm1}{2}$ is the total number of the layers of the top vdW layer. The MSD above is the central result of this work, which is summarized in Fig. 2. It is worth mentioning that in principle $Y = 2$ could also respect mirror symmetry, i.e., AA-stacked bilayer graphene. But, compared to the SLG and ABA trilayer graphene, the AA bilayer graphene is highly unstable in reality. Therefore, it is extremely hard to realize a moiré heterostructure with an AA bilayer in an experiment based on contemporary technique. So, in the main text, we only focus on the experimentally feasible cases, and the cases with AA stacking (e.g., A-AAA-A and AA-A-AA DTMLG) are given in the Appendixes. Note that the rules summarized in Fig. 2 are not valid for AA stacking. In other words, $Y$ should be odd, as indicated above.

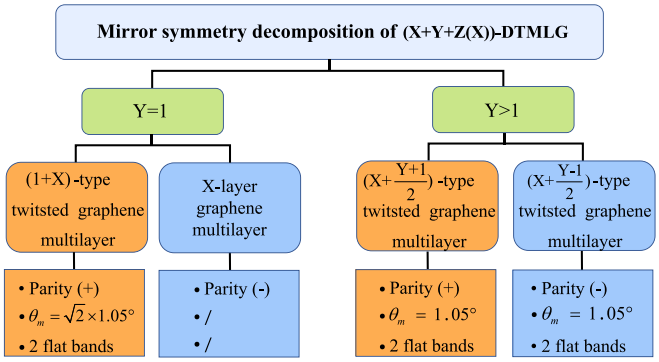


FIG. 2. Classification of the mirror symmetry decomposition (MSD) for a general $(X+Y+Z)$-DTMLG.

Such decomposition will give us several important insights into the essential features of the DTMLGs with mirror symmetry: (1) All the intriguing features of the moiré bands of DTMLG, such as the different magic angles (1.54° or 1.05°) and fourfold degenerate flat bands, can be clearly interpreted by this decomposition. (2) The parity becomes a new discrete degree of freedom of the electrons in DTMLG, and we can define parity-resolved Chern numbers for the moiré flat bands. (3) Such exact mapping strongly implies that the exotic correlation phases observed in twist multilayer graphene (single twist) or multilayer graphene all can exist in the DTMLG systems. (4) Due to the mirror symmetry, the vertical electric field $E_\perp$ acts merely as hybridization terms between the two subsystems and is not directly applied to the subsystems themselves. It thus indicates that $E_\perp$ will affect the correlation states of the subsystems in a rather different way.

The paper is organized as follows. In Sec. II, we first introduce the general continuum Hamiltonian of the DTMLG. Then, we use the $(2+1+2)$-DTMLG and $(1+3+1)$-DTMLG as examples to illustrate the ideas of the MSD in Secs. III and IV, respectively. Then, we derive the decomposition formulas for a general DTMLG in Sec. V. Finally, a short summary is given in Sec. VI.

## II. CONTINUUM HAMILTONIAN OF DTMLG

Based on the continuum model method [77–80], the Hamiltonian of a general $(X+Y+Z)$-DTMLG for one valley and one spin is

$$H_{X+Y+Z}=\begin{pmatrix} H_X(k_1) & T_{XY}^\dagger(r) & 0 \\ T_{XY}(r) & H_Y(k_2) & T_{YZ}^\dagger(r) \\ 0 & T_{YZ}(r) & H_Z(k_3) \end{pmatrix}, \tag{1}$$

where the $H_{X,Y,Z}$ are the Hamiltonian of the bottom, middle, and top vdW layers, i.e., the Hamiltonian of multilayer graphene [70,71,81]. The Brillouin zone of the DTMLG is given in Fig. 1, and $\theta_{XY}=-\theta_{YZ}=\theta$ is the twist angle.

$T_{XY}$ ($T_{YZ}$) describes the moiré hopping between the bottom and middle (middle and top) vdW layers:

$$T_{XY}=\sum_{n=0,1,2} T_{XY}^n e^{iq_n r}, \tag{2}$$

where $q_n=2k_D\sin(\frac{\theta}{2})\exp(i\frac{2n\pi}{3})$. $k_D=\frac{4\pi}{3a_0}$ is the magnitude of the BZ corner wave vector of a single vdW layer, where $a_0=2.46$ Å is the graphene lattice constant,

$$T_{XY}^n=I_{XY}\otimes\begin{pmatrix} \omega_{\rm AA} & \omega_{\rm AB}e^{i\phi_n} \\ \omega_{\rm AB}e^{-i\phi_n} & \omega_{\rm AA}\end{pmatrix}. \tag{3}$$

Here, $I_{XY}$ is a matrix with only one nonzero matrix element. Other parameters are $\phi_n=\text{sign}(\theta_{XY})\frac{2n\pi}{3}$, $\omega_{\rm AA}=0.0797$ eV, $\omega_{\rm AB}=0.0975$ eV. $T_{YZ}$ is given similarly.

## III. MSD OF $(2+1+2)$-DTMLG

Here, we consider the $(2+1+2)$-DTMLG as the first example [70], which is shown in Figs. 1(a) and 1(c). To satisfy the mirror symmetry, the $(2+1+2)$-DTMLG here refers to a (BA-A-AB)-type structure [see Fig. 1(c)], where the moiré interfaces are aligned before twisting. We can see that the middle vdW layer is just SLG, which is also the reflection plane of the mirror symmetry $M_z$.

According to Eq. (1), the explicit form of the Hamiltonian of the $(2+1+2)$-DTMLG is

$$H_0=\begin{pmatrix} H_1 & T_{1,2}^\dagger & 0 & 0 & 0 \\ T_{1,2} & H_2 & \widetilde{T}_{2,3}^\dagger & 0 & 0 \\ 0 & \widetilde{T}_{2,3} & H_3 & \widetilde{T}_{3,4}^\dagger & 0 \\ 0 & 0 & \widetilde{T}_{3,4} & H_4 & T_{4,5}^\dagger \\ 0 & 0 & 0 & T_{4,5} & H_5 \end{pmatrix}. \tag{4}$$

Here, we use the Bloch waves of each SLG $\{|A_i\rangle, |B_i\rangle\}$ as the basis, where $|A_i\rangle$ is the Bloch wave of the A sublattice of the $i$th graphene layer. $H_i(\vec{k})=-v_F[R(\theta_i)(\vec{k}-\vec{K}_i^\xi)]\cdot\vec{\sigma}$ is the Hamiltonian of the $i$th graphene layer, and $R(\theta)$ is the rotation matrix. Since the bottom (top) vdW layer is a BA-type (AB-type) BLG [see Fig. 1(c)], $T_{1,2}$ denotes the interlayer hopping between the first and second graphene layers (AB stacked, no twist)

$$T_{1,2}=\begin{pmatrix} 0 & t_\perp \\ 0 & 0\end{pmatrix}, \tag{5}$$

and $T_{4,5}=T_{1,2}^\dagger$. $\widetilde{T}_{2,3}$ is the moiré interlayer hopping,

$$\widetilde{T}_{2,3}=\sum_{n=0,1,2}\begin{pmatrix} \omega_{\rm AA} & \omega_{\rm AB}e^{i\phi_n} \\ \omega_{\rm AB}e^{-i\phi_n} & \omega_{\rm AA}\end{pmatrix}e^{i\mathbf{q}_n\cdot\mathbf{r}}, \tag{6}$$

which depends on the twist angle $\theta$. $\widetilde{T}_{3,4}$ is given in a similar way. Here, we only consider the nearest-neighbor interlayer hopping and do not include the remote hopping terms for simplicity. Since the remote hopping does not break the mirror symmetry of the crystal structure, it will not affect the MSD here. But, it will slightly change the shape (and the valley Chern number) of the energy bands [8,13].

The idea of MSD in DTMLG is quite like that in the AT-TLG [29,30,34] as well as the ABA-stacked trilayer graphene [82,83]. Namely, we build a different basis that satisfies mirror symmetry. Based on this different basis, the Hamiltonian (4) can be decoupled into two subsystems with opposite parity. Because the middle graphene layer is the mirror reflection plane, we see that the first (second) and the fifth (fourth) graphene layers are exactly aligned, as shown in Fig. 1(c). Thus, a natural choice is $\{|A_{1,5},+\rangle, |B_{1,5},+\rangle, |A_{2,4},+\rangle, |B_{2,4},+\rangle, |A_3\rangle, |B_3\rangle, |A_{2,4},-\rangle, |B_{2,4},-\rangle, |A_{1,5},-\rangle, |B_{1,5},-\rangle\}$,

where

$$|A_{1,5},+\rangle = \frac{1}{\sqrt{2}}(|A_1\rangle + |A_5\rangle),$$
$$|A_{1,5},-\rangle = \frac{1}{\sqrt{2}}(|A_1\rangle - |A_5\rangle). \quad (7)$$

Here, $|A_{1,5},\pm\rangle$ are the two parity-resolved basis functions coming from the A sublattice of the first and fifth graphene layers, where $+$ $(-)$ denotes the even (odd) parity. And, $|B_{1,5},\pm\rangle$ are for the B sublattice accordingly. Meanwhile, $|A_{2,4},\pm\rangle$ and $|B_{2,4},\pm\rangle$ correspond to the second and fourth graphene layers, which are defined in the same way. This parity-resolved basis gives rise to a unitary transformation,

$$U = \frac{1}{\sqrt{2}}\begin{pmatrix} I & 0 & 0 & 0 & I \\ 0 & I & 0 & I & 0 \\ 0 & 0 & \sqrt{2}I & 0 & 0 \\ 0 & I & 0 & -I & 0 \\ I & 0 & 0 & 0 & -I \end{pmatrix}, \quad (8)$$

where $I$ is a $2\times 2$ identity matrix. Under this transformation, $H_{\rm mirr} = U^{-1}H_0U$, where

$$H_{\rm mirr} = \begin{pmatrix} H_{\rm TMBG} & 0 \\ 0 & H_{\rm BLG} \end{pmatrix} = \begin{pmatrix} H_1 & T_{1,2}^\dagger & 0 & 0 & 0 \\ T_{1,2} & H_2 & \sqrt{2}\widetilde{T}_{2,3}^\dagger & 0 & 0 \\ 0 & \sqrt{2}\widetilde{T}_{2,3} & H_3 & 0 & 0 \\ 0 & 0 & 0 & H_2 & T_{1,2} \\ 0 & 0 & 0 & T_{1,2}^\dagger & H_1 \end{pmatrix}. \quad (9)$$

We see that $H_{\rm mirr}$ is decoupled into two subsystems: $H_{\rm TMBG}$ and $H_{\rm BLG}$. Importantly, $H_{\rm TMBG}$ is exactly equivalent to the Hamiltonian of TMBG [8,11,12,22,84–87], except that the moiré interlayer hopping is multiplied by a factor of $\sqrt{2}$, i.e., $\sqrt{2}\widetilde{T}_{2,3}$. $H_{\rm BLG}$ is precisely equal to the Hamiltonian of a BLG. Meanwhile, according to the parity-resolved basis, $H_{\rm TMBG}$ is of even parity, while the $H_{\rm BLG}$ belongs to odd parity.

Such decomposition clearly interprets the moiré band structure of the $(2+1+2)$-DTMLG. It is known that a TMBG has a pair of flat bands at the magic angle 1.05°, gapped from other high-energy bands [8]. However, in $H_{\rm TMBG}$ above, because the factor $\sqrt{2}$ in moiré interlayer hopping, it is expected that the magic angle now should be $\sqrt{2}\times 1.05^\circ \approx 1.54^\circ$ like that in ATTLG [29,30]. Meanwhile, due to the $H_{\rm BLG}$, we also expect that there should be a pair of parabolic bands like that in BLG touching at the $K_{tb}$ point. Then, we plot the energy bands of $H_{\rm mirr}$ in Figs. 3(a) and 3(b), which is consistent with our former numerical results [70]. The blue (red) solid lines represent the even-parity (odd-parity) bands. In Fig. 3(b), we do find a perfect flat band (even parity) coexisting with a pair of parabolic bands (odd parity) at $\theta = 1.54^\circ$, which coincides well with the MSD above.

The MSD also indicates that the electrons here now have three discrete degrees of freedom, i.e., spin, valley, and parity (even or odd). It thus becomes possible to define a parity-dependent Chern number for the flat bands. As shown in Fig. 3(b), the two flat bands near $E_f$ come from an equivalent TMBG, i.e., $H_{\rm TMBG}$, which are of even parity. Meanwhile,

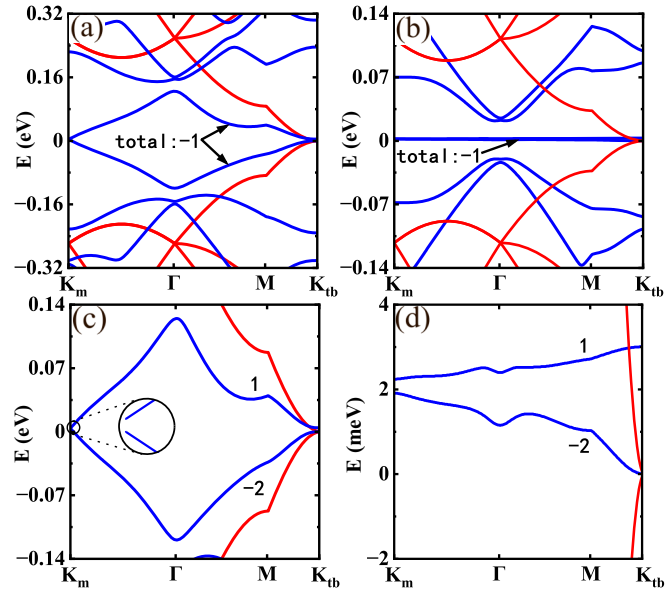


FIG. 3. Band structure of the $(2+1+2)$-DTMLG with mirror symmetry. (a) For $\theta = 2.65^\circ$; (b) for $\theta = 1.54^\circ$; (c) and (d) are enlarged views of the flat bands in (a) and (b), respectively. Blue (red) solid lines represent the band structure of TMBG (BLG), and the black numbers indicate the Chern numbers for the energy bands.

the two parabolic bands are of odd parity. So, though the flat bands and the parabolic bands degenerate at the $K_{tb}$ point, we can study their topological features separately. It is known that a TMBG has two topological flat bands, each of which has a nonzero valley Chern number [8]. And, different from TBG, the two flat bands in TMBG are not degenerate at the Dirac points, due to the lack of $C_2T$ symmetry. All these unique features of the flat bands are reserved in the $(2+1+2)$-DTMLG because of the exact mapping between $H_{\rm TMBG}$ and a real TMBG. Figures 3(c) and 3(d) are the enlarged view of the flat bands in Figs. 3(a) and 3(b), respectively. Although the magic angle now is larger, the two flat bands have nonzero valley Chern numbers, namely, that of the upper (lower) flat band is 1 $(-2)$, which are the same as that in a real TMBG at the magic angle 1.05° [8]. As for the $H_{\rm BLG}$, we can exclusively calculate the Berry curvature of the parabolic bands, which is the same as that of the BLG.

Now, we discuss the influence of the perpendicular electric field $E_\perp$. Since that $E_\perp$ does not commute with $M_z$, it does not directly act on $H_{\rm TMBG}$ and $H_{\rm BLG}$ but works as the hybridization terms between the two subsystems [34]. In the parity-resolved basis, the Hamiltonian of $E_\perp$ is

$$H_V = \begin{pmatrix} 0 & D \\ D^\dagger & 0 \end{pmatrix}, \quad (10)$$

$$D = \begin{pmatrix} 0 & 2VI \\ VI & 0 \\ 0 & 0 \end{pmatrix}, \quad (11)$$

where $D$ is the hybridization matrix, $V$ is the potential difference between adjacent layers, and $I$ is a $2\times 2$ identity matrix. Here, we assume that the $E_\perp$ induced potential will be uniformly distributed among the graphene layers. Clearly, $H_V$ indicates that the $E_\perp$ has different ways to couple with a real

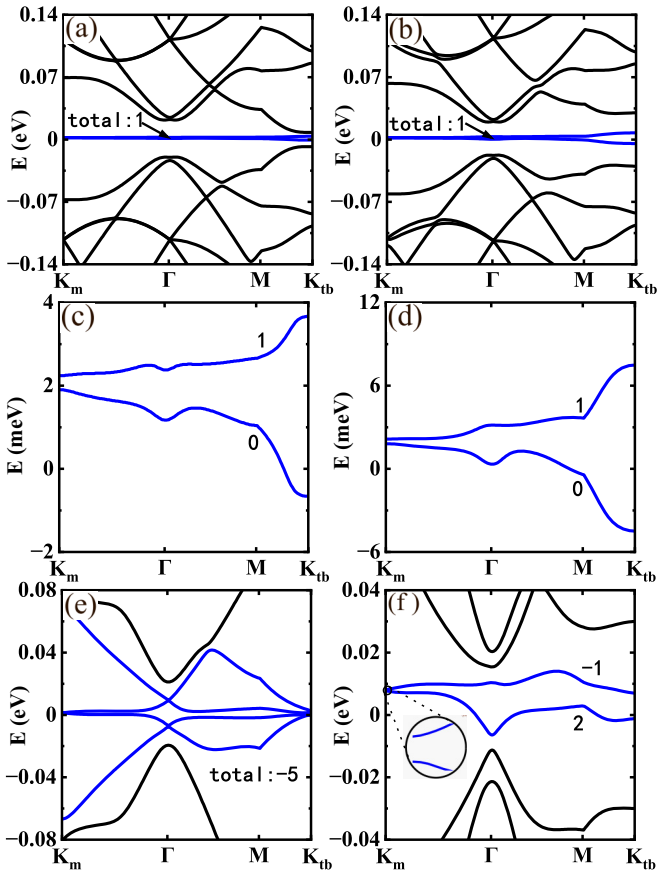


FIG. 4. Band structures of the $(2+1+2)$-DTMLG at $\theta = 1.54°$ in the presence of $E_\perp$ or lateral shift. (a) $V = 4$ meV. (b) $V = 15$ meV. (c), (d) The enlarged view of the flat bands in (a) and (b), respectively. (e), (f) Show the energy bands of the $H_{\mathrm{BA+A+CA}}$ after sliding, where (e) $V = 0$ meV and (f) $V = 15$ meV.

TMBG and with the subsystem $H_{\mathrm{TMBG}}$, though they have the same Hamiltonian in form. In a real TMBG, $E_\perp$ will shift the energy of the states at $K_m$ and $K_{tb}$ towards opposite directions, separate the two flat bands, and change their valley Chern number [8]. However, in the $(2+1+2)$-DTMLG here, $E_\perp$ merely works as the hybridization between the two subsystems and thus has a completely different influence. First of all, due to $E_\perp$, the parity is no longer a good quantum number now. In Figs. 4(a) and 4(b), we plot the moiré bands of the $(2+1+2)$-DTMLG in the presence of $E_\perp$. We see that, once an $E_\perp$ is applied, the degeneracy of the parabolic bands at $K_{tb}$ point is broken immediately, and the central two flat bands are isolated from other bands by an obvious gap. Meanwhile, $E_\perp$ will induce a hybridization between the flat bands and other odd-parity bands, which changes their Chern numbers at once. We zoom on the flat bands in Figs. 4(c) and 4(d), which show that the Chern number of the lower flat band is changed from $-2$ to 0. It should be noted that $E_\perp$ has little effect on the states near the $K_m$ point. The gap between the two flat bands at $K_m$ is still very tiny, even if a large $E_\perp$ is applied. Another distinct feature is that the effects of $E_\perp$ are irrelative to the direction of $E_\perp$ because of the mirror symmetry of $(2+1+2)$-DTMLG. It is different from the case of TMLG, where the top SLG and bottom BLG are asymmetric [8].

The lateral shift of the moiré interface plays an important role in the ATTLG and DTMLG systems, which not only breaks the mirror symmetry but also significantly modifies the band structures [32,35]. So far, accurate control of the lateral shift in moiré heterostructure is still impossible. Here, the MSD above also can give some insight into the lateral shift. As shown in Fig. 1, we always assume that the graphene layers of a moiré interface are aligned when $\theta = 0$. For example, the $(2+1+2)$-DTMLG above has a (BA + A + AB)-type configuration. If the top vdW layer is shifted, we then get a (BA + A + CA)-DTMLG. To get the Hamiltonian of (BA + A + CA)-DTMLG, we only need to replace the $\widetilde{T}_{34}$ in Eq. (4) by $\widetilde{T}'_{34}$ accordingly,

$$\widetilde{T}'^{\dagger}_{34} = \sum_{n=0,1,2} \begin{pmatrix} \omega_{\mathrm{AA}} & \omega_{\mathrm{AB}} e^{i\phi_n} \\ \omega_{\mathrm{AB}} e^{-i\phi_n} & \omega_{\mathrm{AA}} \end{pmatrix} e^{i(\mathbf{q}_n \cdot \mathbf{r} + \phi_n)}. \tag{12}$$

With the same unitary transformation, we get $H_{\mathrm{BA+A+CA}} = H_{\mathrm{mirr}} + H_{\mathrm{shift}}$, where all the effects of lateral shift are attributed to $H_{\mathrm{shift}}$:

$$H_{\mathrm{shift}} = \begin{pmatrix} 0 & 0 & 0 & 0 & 0 \\ 0 & 0 & -\widetilde{T}'^{\dagger} & 0 & 0 \\ 0 & -\widetilde{T}' & 0 & \widetilde{T}' & 0 \\ 0 & 0 & \widetilde{T}'^{\dagger} & 0 & 0 \\ 0 & 0 & 0 & 0 & 0 \end{pmatrix}. \tag{13}$$

Here, $\widetilde{T}' = \frac{\sqrt{2}}{2}(\widetilde{T}_{2,3} - \widetilde{T}'^{\dagger}_{3,4})$. In the mirror symmetric (BA + A + AB) configuration, $\widetilde{T}_{2,3} = \widetilde{T}^{\dagger}_{3,4}$ and thus $\widetilde{T}' = 0$. But for the (BA + A + CA) configuration after sliding, $\widetilde{T}_{2,3} \neq \widetilde{T}'^{\dagger}_{3,4}$, so that $\widetilde{T}'$ becomes nonzero. In fact, the $\widetilde{T}'$ represents the effects of lateral shift. It not only appears in the hybridization terms to break the mirror symmetry, but also occurs in the even-parity block. Therefore, the influence of lateral shift is more complicated than that of the $E_\perp$. In Fig. 4(e), we plot the band structure of the (BA + A + CA) configuration after sliding. We see that the two flat bands and two parabolic bands are heavily hybridized, but we still can get a large DOS at $E_f$. Meanwhile, the central four bands near $E_f$ are isolated from other high-energy bands, and their total valley Chern number is $-5$. Very interestingly, when we apply a proper electric field $E_\perp$ (3 meV $< V <$ 65 meV) on the (BA + A + CA) configuration, we eventually get a pair of flat bands isolated from other bands with nonzero valley Chern number, quite like that in the (BA + A + AB) configuration [see Fig. 4(f)].

## IV. MSD OF (1 + 3 + 1)-DTMLG

Then, we discuss the case of $(1+3+1)$-DTMLG [71]. Compared with the $(2+1+2)$-DTMLG above, the middle vdW layer now becomes Bernal-stacked trilayer graphene, but the middle SLG is still a mirror reflection plane (see Fig. 1).

Based on Eq. (1), The Hamiltonian of $(1+3+1)$-DTMLG is

$$H_0 = \begin{pmatrix} H_1 & \widetilde{T}^{\dagger}_{12} & 0 & 0 & 0 \\ \widetilde{T}_{12} & H_2 & T^{\dagger}_{23} & 0 & 0 \\ 0 & T_{23} & H_3 & T^{\dagger}_{34} & 0 \\ 0 & 0 & T_{34} & H_4 & \widetilde{T}^{\dagger}_{45} \\ 0 & 0 & 0 & \widetilde{T}_{45} & H_5 \end{pmatrix}. \tag{14}$$

Note that the moiré interlayer hopping now is $\widetilde{T}_{1,2}$ ($\widetilde{T}_{4,5}$), which exists between the first (fourth) and second (fifth) graphene layers.

Since the middle graphene layer is still the mirror reflection plane, we can still use the parity-resolved basis in the last section to do the MSD. After the unitary transformation, we get

$$H_{\text{mirr}} = \begin{pmatrix} H'_{\text{TMBG}} & 0 \\ 0 & H_{\text{TBG}} \end{pmatrix} = \begin{pmatrix} H_1 & \widetilde{T}^{\dagger}_{1,2} & 0 & 0 & 0 \\ \widetilde{T}_{1,2} & H_2 & \sqrt{2}T^{\dagger}_{2,3} & 0 & 0 \\ 0 & \sqrt{2}T_{2,3} & H_3 & 0 & 0 \\ 0 & 0 & 0 & H_2 & \widetilde{T}_{1,2} \\ 0 & 0 & 0 & \widetilde{T}^{\dagger}_{1,2} & H_1 \end{pmatrix}. \quad (15)$$

Here, we see that the $(1+3+1)$-DTMLG is mapped into two subsystems: an equivalent TMBG $H'_{\text{TMBG}}$ (even parity) and an equivalent TBG $H_{\text{TBG}}$ (odd parity). The two subsystems here are different from that of the $(2+1+2)$-DTMLG. First, the even-parity part $H'_{\text{TMBG}}$ in Eq. (15) here is distinct from the $H_{\text{TMBG}}$ in Eq. (9). It is because the $\sqrt{2}$ factor is now at the interlayer hopping without twist, instead of the moiré interlayer hopping like in Eq. (9). Therefore, in $(2+1+2)$-DTMLG, the magic angle of the subsystem $H_{\text{TMBG}}$ is $\sqrt{2}\times 1.05^\circ$, but the magic angle of the $H'_{\text{TMBG}}$ in the $(1+3+1)$-DTMLG is still $1.05^\circ$. Further numerical calculations show that the enlarged term $\sqrt{2}T_{2,3}$ has little influence on the bands near $E_f$. Second, the odd-parity block $H_{\text{TBG}}$ now has a moiré interface and becomes an equivalent TBG, which thus will also give rise to a pair of flat bands at the magic angle $1.05^\circ$. So, in $(1+3+1)$-DTMLG, we get two pairs of flat bands at the magic angle $1.05^\circ$, where one pair is of even parity and the other is of odd parity. The MSD here gives a clear interpretation of the fourfold degenerate flat bands first reported in our previous work [71]. Interestingly, the AT-NLG also can be decoupled into several copies of TBGs, but their magic angles are different [29,34]. In that case, we cannot get two pairs of flat bands at the same time [66,67].

In Figs. 5(a) and 5(b), we plot the energy bands of the $(1+3+1)$-DTMLG at two different twisted angles, where blue (red) lines represent the even-parity (odd-parity) bands from $H'_{\text{TMBG}}$ ($H_{\text{TBG}}$). At $1.05^\circ$, we do observe the fourfold degenerate flat bands [see Fig. 5(b)]. Similar to the $(2+1+2)$-DTMLG, we can also define a parity-dependent valley Chern number for the fourfold flat bands. In Figs. 5(c) and 5(d), we zoom in on the flat bands. As we expected, the two flat bands from $H'_{\text{TMBG}}$ (blue lines) have tiny gaps at the $K_m$ and $K_{tb}$ points, which is the typical feature of the flat bands in TMBG [8]. Meanwhile, such two flat bands have a nonzero valley Chern number as well, which is also the same as that in TMBG. As for the two flat bands from $H_{\text{TBG}}$ (red lines), they are topological trivial and degenerate at the $K_m$ and $K_{tp}$ points, which is the same as that in TBG.

In the parity-resolved basis, the Hamiltonian of $E_\perp$, i.e., $H_V$, has the same form as that of the $(2+1+2)$-DTMLG [see Eq. (10)]. $E_\perp$ breaks the mirror symmetry and acts as hybridization terms between the even- and odd-parity blocks,

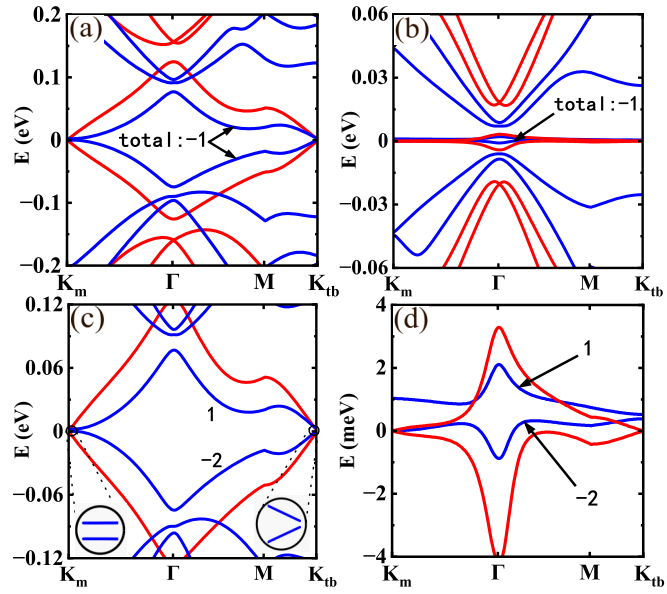


FIG. 5. Band structures of the $(1+3+1)$-DTMLG with mirror symmetry. (a) $\theta = 2.0^\circ$, (b) $\theta = 1.05^\circ$. (c), (d) The enlarged view of the flat bands in (a) and (b), respectively. Blue (red) solid lines represent the band structure of TMBG (BLG), and the black numbers indicate the Chern numbers for the energy bands.

which is similar to that in $(2+1+2)$-DTMLG. In Figs. 6(a) and 6(b), we plot the moiré bands of the $(1+3+1)$-DTMLG at $1.05^\circ$ with $V = 4$ meV and $V = 10$ meV, respectively. And we zoom in on flat bands in Figs. 6(c) and 6(d). Although the $(1+3+1)$-DTMLG is decoupled into an equivalent TMBG and an equivalent TBG, the influence of the $E_\perp$ is rather different from that in real TMBG and TBG. First, as mentioned above, parity is no longer a good quantum number once $E_\perp$ is applied. Meanwhile, the hybridization breaks the flat-band degeneracy of the $H_{\text{TBG}}$ at the $K_{tb}$ point. In contrast, in a real TBG, we know that an electric field cannot lift the degeneracy of flat bands at the Dirac points. Due to the mirror symmetry, the moiré bands in the $(1+3+1)$-DTMLG are unrelated to the direction of $E_\perp$ as well, i.e., $\pm V$ give rise to the same moiré band structures. Furthermore, $E_\perp$ also can change the Chern number of the flat bands, as shown in Figs. 6(c) and 6(d). Figures 6(b) and 6(d) further indicate that, when V is large enough, the outermost two flat bands will overlap with the high-energy bands in energy.

We then discuss the effects of the lateral shift. Here, with a lateral shift, we get an (A + ABA + C) configuration, in which the top vdW layer is shifted. In the parity-resolved basis, the effects of the lateral shift can be attributed to a shift term $H_{\text{shift}}$:

$$H_{\text{shift}} = \frac{1}{\sqrt{2}} \times \begin{pmatrix} 0 & -\widetilde{T}'^{\dagger} & 0 & \widetilde{T}'^{\dagger} & 0 \\ -\widetilde{T}' & 0 & 0 & 0 & \widetilde{T}' \\ 0 & 0 & 0 & 0 & 0 \\ \widetilde{T}' & 0 & 0 & 0 & -\widetilde{T}' \\ 0 & \widetilde{T}'^{\dagger} & 0 & -\widetilde{T}'^{\dagger} & 0 \end{pmatrix}, \quad (16)$$

where $H_{\text{A+ABA+C}} = H_{\text{mirr}} + H_{\text{shift}}$ and $H_{\text{mirr}}$ is the Hamiltonian of the (A + ABA + A) configuration. From $H_{\text{shift}}$, we see that the lateral shift will not only give rise to hybridization

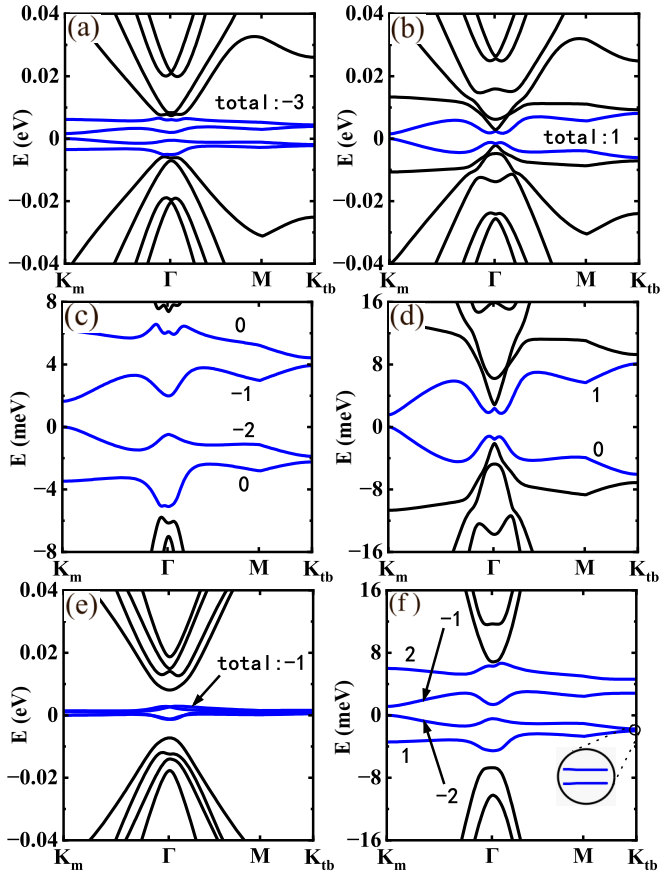


FIG. 6. Band structures of the $(1+3+1)$-DTMLG at $\theta = 1.05^\circ$ in the presence of $E_\perp$ or lateral shift. (a) $V = 4$ meV, (b) $V = 10$ meV. (c), (d) The enlarged view of the flat bands in (a) and (b), respectively. (e), (f) Show the energy bands of the $H_{\mathrm{A+ABA+C}}$ after sliding, where (e) $V = 0$ meV and (f) $V = 4$ meV.

between the even- and odd-parity blocks but also have direct effects on the two subsystems. In Figs. 6(e) and 6(f), we plot the moiré bands of the (A + ABA + C)-DTMLG at the magic angle, with $V = 0$ and 4 meV, respectively. Although the high-energy bands are changed, we still get four nearly degenerate flat bands and $E_\perp$ also can lift the degenerate of the four flat bands.

## V. MSD OF A GENERAL DTMLG

Similar to the two examples above, we actually can give a simple decomposition scheme for a general DTMLG with mirror symmetry. As mentioned above, we consider a general $(X+Y+X)$-DTMLG with mirror symmetry. For convenience, we first rewrite the Hamiltonian of Eq. (1),

$$H_0 = \begin{pmatrix} H_{\mathrm{down}} & T_{dm}^\dagger & 0 \\ T_{dm} & H_N & T_{um}^\dagger \\ 0 & T_{um} & H_{up} \end{pmatrix}. \tag{17}$$

Here, we define $N = X + \frac{Y+1}{2}$, so that the middle SLG, i.e., the mirror reflection plane, is just the $N$th graphene layer from bottom to top. $H_N$ here is the Hamiltonian of the middle SLG. Why we treat the middle SLG individually here is to facilitate constructing a proper basis. Then, all the graphene layers above (below) the middle graphene layer are described by $H_{up}$ ($H_{\mathrm{down}}$), which is a $(2X+Y-1)\times(2X+Y-1)$ matrix. $T_{um}$ ($T_{dm}$) denote the hybridization between $H_{\mathrm{up}}$ ($H_{\mathrm{down}}$) and $H_N$.

Considering the position of the moiré interlayer hopping, there are two different cases depending on whether $Y = 1$ or not. $Y = 1$ means that the middle vdW layer is just an SLG, where the $(2+1+2)$-DTMLG is the simplest example. In this situation, the moiré interlayer hopping is in $T_{um}$ and $T_{dm}$, where

$$T_{dm} = (0 \quad \dots \quad 0 \quad \widetilde{T}_{N,N-1}), \tag{18}$$

$$T_{um}^\dagger = (\widetilde{T}_{N,N+1}^\dagger \quad 0 \quad \dots \quad 0) \tag{19}$$

and

$$H_{\mathrm{down}} = \begin{pmatrix} H_1 & T_{1,2}^\dagger & \cdots & 0 \\ T_{1,2} & H_2 & \cdots & \vdots \\ \vdots & \ddots & \ddots & \vdots \\ 0 & \cdots & T_{N-2,N-1} & H_{N-1} \end{pmatrix}, \tag{20}$$

$$H_{\mathrm{up}} = \begin{pmatrix} H_{N+1} & T_{N+1,N+2}^\dagger & \cdots & 0 \\ \vdots & \ddots & \ddots & \vdots \\ \vdots & \cdots & H_{L-1} & T_{L-1,L}^\dagger \\ 0 & \cdots & T_{L-1,L} & H_L \end{pmatrix}. \tag{21}$$

For convenience, we define $L = 2X + Y$ as the total layer number of the DTMLG. When $Y > 1$, e.g., $(1+3+1)$-DTMLG, the moiré interlayer hopping is in $H_{\mathrm{up}}$ and $H_{\mathrm{down}}$. So, we have

$$T_{dm} = (0 \quad \dots \quad 0 \quad T_{N,N-1}), \tag{22}$$

$$T_{um}^\dagger = (T_{N,N+1}^\dagger \quad 0 \quad \dots \quad 0) \tag{23}$$

and now

$$H_{\mathrm{down}} = \begin{pmatrix} H_1 & T_{1,2}^\dagger & \cdots & \cdots & 0 \\ \vdots & \ddots & \ddots & \ddots & \vdots \\ \vdots & T_{X-1,X} & H_X & \widetilde{T}_{X,X+1}^\dagger & \vdots \\ \vdots & \ddots & \ddots & \ddots & \vdots \\ 0 & \cdots & \cdots & T_{N-2,N-1} & H_{N-1} \end{pmatrix}, \tag{24}$$

$$H_{\mathrm{up}} = \begin{pmatrix} H_{N+1} & T_{N+1,N+2}^\dagger & \cdots & \cdots & 0 \\ \vdots & \ddots & \ddots & \ddots & \vdots \\ \vdots & T_{X+Y-1,X+Y} & H_{X+Y} & \widetilde{T}_{X+Y,X+Y+1}^\dagger & \vdots \\ \vdots & \ddots & \ddots & \ddots & \vdots \\ 0 & \cdots & \cdots & T_{L-1,L} & H_L \end{pmatrix}. \tag{25}$$

The moiré interlayer hoppings now are the terms $\widetilde{T}_{X,X+1}$ and $\widetilde{T}_{X+Y,X+Y+1}$. The two cases above will give different results after the MSD.

Then, we can construct a set of parity-resolved bases:

$$\begin{aligned} |A_{i,L+1-i}, +\rangle &= \frac{1}{\sqrt{2}}(|A_i\rangle + |A_{L+1-i}\rangle), \\ |A_{i,L+1-i}, -\rangle &= \frac{1}{\sqrt{2}}(|A_i\rangle - |A_{L+1-i}\rangle), \\ |A_N, +\rangle &= |A_N\rangle, \\ |B_N, +\rangle &= |B_N\rangle, \end{aligned} \tag{26}$$

where $i \in \{1, 2, \ldots, N-1\}$ and $\pm$ denote the parity. For example, when $i = 1$, we get $|A_{1,L}, +\rangle = \frac{1}{\sqrt{2}}(|A_1\rangle + |A_L\rangle)$, which is obviously of even parity considering the mirror symmetry. Similarly, the wave function $|A_{1,L}, -\rangle$ is of odd parity. $|A_N, +\rangle$ and $|B_N, +\rangle$ are the wave functions of the middle graphene layer, which should be of even parity. With the definitions above, we get a set of parity-resolved bases, i.e., $\{|+\rangle, |-\rangle\}$, where the even-parity basis is $|+\rangle = \{|A_{1,L}, +\rangle, |B_{1,L}, +\rangle, |A_{2,L-1}, +\rangle, |B_{2,L-1}, +\rangle, \ldots, |A_{N-1,N+1}, +\rangle, |B_{N-1,N+1}, +\rangle, |A_N, +\rangle, |B_N, +\rangle\}$ and the odd-parity basis is $|-\rangle = \{|A_{N-1,N+1}, -\rangle, |B_{N-1,N+1}, -\rangle, \ldots, |A_{2,L-1}, -\rangle, |B_{2,L-1}, -\rangle, |A_{1,L}, -\rangle, |B_{1,L}, -\rangle\}$.

In such basis, the $H_0$ in Eq. (17) can be decoupled by a unitary transformation

$$H_{\text{mirr}} = U^{-1} H_0 U = \begin{pmatrix} H_+ & 0 \\ 0 & H_- \end{pmatrix}. \tag{27}$$

The $H_+$ ($H_-$) is the even- (odd-) parity block

$$H_+ = \begin{pmatrix} H_{\text{down}} & \sqrt{2}T_{dm}^\dagger \\ \sqrt{2}T_{dm} & H_N \end{pmatrix},$$
$$H_- = H_{\text{up}}, \tag{28}$$

The detailed derivation is given in the Appendix. Note that, though the $H_{\text{down}}$ and $H_{\text{up}}$ in $H_{\text{mirr}}$ above have the same form as that in Eqs. (20), (21), (24), and (25), they correspond to the parity-resolved basis, instead of the original Bloch wave basis. Now, we see that the DTMLG with mirror symmetry can always be decoupled into two subsystems with opposite parity, i.e., $H_+$ and $H_-$. As mentioned above, depending on whether the middle vdW layer is an SLG or not, there are two distinct situations in which the $H_+$ and $H_-$ correspond to different concrete systems. The reason is where the moiré interlayer hopping is.

When $Y = 1$, the moiré interlayer hopping is in $T_{dm}$ and $T_{um}$, as shown in Eqs. (18) and (19). So, $H_- = H_{\text{up}}$ does not have moiré interlayer hopping [see Eq. (21)]. Namely, $H_-$ is just an equivalent multilayer graphene system, which has the same stacking order as the top vdW layer. For example, in $(2+1+2)$-DTMLG, $H_-$ is just a bilayer graphene (AB stacking). Meanwhile, from Eqs. (28), (18), and (19), we can see that $H_+$ now describes a $(1+X)$-type twisted multilayer graphene (single twist) [9,18,81,88] with a $\sqrt{2}$ scaled moiré interlayer hopping. It implies that $H_+$ should have a pair of flat bands at the magic angle $\sqrt{2} \times 1.05^\circ$. This is also in accordance with the $(2+1+2)$-DTMLG where $H_+$ is equivalent to a TMBG with a $\sqrt{2} \times 1.05^\circ$ magic angle.

When $Y > 1$, the moiré interlayer hopping is in $H_{\text{down}}$ and $H_{\text{up}}$, as shown in Eqs. (24) and (25). Thus, $H_- = H_{\text{up}}$ now correspond to a $(X + \frac{Y-1}{2})$-type twisted multilayer graphene [see Eq. (25) and definition of $H_{\text{up}}$]. An example is the $(1+3+1)$-DTMLG with $Y = 3$ and $X = 1$. In this example, $H_-$ is equal to a TBG, i.e., $(1+1)$ type, which coincides with the general decomposition formula above. Then, we discuss $H_+$. From Eqs. (28), (22), and (23), we see that the hopping between $H_N$ and $H_{\text{down}}$ is a normal interlayer hopping between graphene layers, instead of the moiré one. It implies that $H_+$ now describes a $(X + \frac{Y+1}{2})$-type twisted multilayer graphene with a single-twist angle. In the example of $(1+3+1)$-DTMLG, $H_+$ thus becomes a TMBG, i.e., $(1+2)$ type. Here, since the $\sqrt{2}$ factor is not at the moiré interlayer hopping, both $H_-$ and $H_+$ should have a pair of flat bands at the magic angle $1.05^\circ$. Because the moiré band structures of twisted multilayer graphene are known [9,18,81,88], the band structure of such DTMLG with mirror symmetry can be well understood from the MSD, namely, from the behaviors of $H_+$ and $H_-$.

With parity-resolved basis, the perpendicular electric field can be described as hybridization terms between $H_+$ and $H_-$ since it breaks the mirror symmetry. The Hamiltonian of $E_\perp$ is

$$H_V = \begin{pmatrix} 0 & D \\ D^\dagger & 0 \end{pmatrix}, \tag{29}$$

where $H = H_{\text{mirr}} + H_V$. $D$ is now a $(2X+Y+1) \times (2X+Y-1)$ matrix

$$D = \begin{pmatrix} \Delta \\ 0 \end{pmatrix} \tag{30}$$

and $\Delta$ is a $(X + \frac{Y-1}{2}) \times (X + \frac{Y-1}{2})$ block matrix, where each block $\Delta_{i,j} = V(N-i) I \delta_{i,N-j}$ is $2 \times 2$ matrix. As defined before, $V$ is the potential difference between adjacent graphene layers. Clearly, the $H_V$ indicates that $E_\perp$ will not directly act on the $H_+$ and $H_-$, but works as the hybridization between $H_+$ and $H_-$.

In short, according to the discussions above, the MSD can be summarized in a schematic in Fig. 2.

## VI. SUMMARY

We theoretically reveal that a general $(X+Y+Z)$-DTMLG with mirror symmetry can be exactly decoupled into two subsystems, i.e., $H_+$ and $H_-$, with opposite parity, by constructing a parity-resolved basis. Such MSD can be classified into two categories, depending on whether the middle vdW layer is an SLG ($Y = 1$) or not.

When $Y = 1$, the DTMLG is mapped into a $(1+X)$-type twisted multilayer graphene (single twist, even parity) and an $X$-layer graphene multilayer (no twist, odd parity). Since the moiré interlayer hopping is scaled by a factor of $\sqrt{2}$, the $(1+X)$-twisted multilayer graphene has an enlarged magic angle $\sqrt{2} \times 1.05^\circ$. The $(2+1+2)$-DTMLG is the simplest example for this case, which can be decoupled into an equivalent TMBG and an equivalent bilayer graphene. The MSD can give a clear interpretation of the moiré band structure of the $(2+1+2)$-DTMLG. For example, since the $H_+$ is equal to a TMBG, the $(2+1+2)$-DTMLG has a pair of topological flat bands with nonzero valley Chern number, which is exactly the same as the case of TMBG, but appears at a larger magic angle.

When $Y > 1$, the DTMLG is mapped into two twisted multilayer graphenes: a $(X + \frac{Y+1}{2})$-type (single twist, even parity) and a $(X + \frac{Y-1}{2})$-type (single twist, odd parity). Here, the moiré interlayer hopping does not have the $\sqrt{2}$ factor, so the two subsystems both can give rise to a pair of flat bands at the magic angle $1.05^\circ$. In other words, we can get fourfold degenerate flat bands in this case. The $(1+3+1)$-DTMLG is the simplest example for this case, in which $H_+$ is equal to a TMBG, and $H_-$ is equal to a TBG. According to the MSD, we can well understand the behaviors of the fourfold degenerate

flat bands here. The two flat bands from TMBG are of even parity and have nonzero valley Chern numbers. Meanwhile, the two from the TBG are of odd parity and are topological trivial [71].

The MSD indicates that the perpendicular electric field $E_\perp$ will act as hybridization terms between $H_+$ and $H_-$ since $E_\perp$ breaks the mirror symmetry. In other words, $E_\perp$ here has a different way to couple with the DTMLG, distinct from the single-twist moiré heterostructures.

Most importantly, the MSD implies that all the novel correlated states observed in the twisted multilayer graphene systems (e.g., TBG [1–3,56], TMBG [22,84–87], twisted double-bilayer graphene [17,89–92], etc.) as well as the multilayer graphene (e.g.. bilayer graphene [93–95]) can also exist in the DTMLG system since their Hamiltonians are exactly equivalent. It is quite like the case of ATTLG, which can be decoupled into a TBG and SLG. Since the superconducting state is observed in TBG, it is expected that the superconducting state should also exist in ATTLG, which is finally confirmed in recent experiments. Thus, according to the MSD above, we expect that similar to the TBG case, the superconducting state should exist in the $(1+3+1)$-DTMLG. Meanwhile, due to the mirror symmetry, the parity (even or odd) becomes a new discrete degree of freedom of the electrons in the DTMLG, in addition to the spin and valley. Thus, in principle, we may also expect that some new correlated states, which spontaneously break the parity degree of freedom, can exist in the DTMLG systems. One possible system is the $(1+3+1)$-DTFLG, where the parity-polarized states may exist in the fourfold degenerate flat bands when the Coulomb interaction is considered.

The MSD can give some further expectations about the properties of the DTMGL system. The first one is the effect of electron correlations. It is known that, due to the strong influence of Coulomb interaction, the shape of flat bands in magic-angle TBG [96–100] (as well as magic-angle ATTLG [50]) is very sensitive to the doping. In contrast, in twisted double-bilayer graphene [101,102] (TMBG [103] and twisted mono-trilayer graphene [103,104]), the influence of the Coulomb interaction is strongly suppressed. So, for the $(1+3+1)$-DTMLG, since its odd parity part is equivalent to a TBG, the Coulomb interaction should significantly change the flat bands when away from half-filling. Meanwhile, the Coulomb interaction may have little effect on the even-parity party (i.e., TMBG). We expect the situation to be similar in other DTMLGs with mirror symmetry. The second one is the electron-phonon coupling. Previous literature has shown that the strength of the electron-phonon coupling is very large in magic-angle TBG and magic-angle ATTLG, while it is rather weak in TMBG and twisted double-bilayer graphene [53,62,105]. A rather interesting question is whether similar effects are also present in the DTMLG with mirror symmetry, which deserves further efforts in the future.

Finally, it should be noted that mirror symmetry should exist in most double-twisted moiré systems (alternating twist), in addition to the ones mentioned in this paper. For example, the boron nitride(BN)/graphene/BN moiré structure has already been realized in experiment [106–108] (mirror symmetry exists only when the relative orientation of the two BN layers is $0^\circ$). On the one hand, mirror symmetry can be controlled by the twist angle, which offers an intriguing way to manipulate symmetry-related electronic properties. On the other hand, a similar MSD may also exist in these systems [109,110], which may be an interesting issue to be explored in further studies.

*Note added.* In this paper, our decomposition method depends on mirror symmetry and gives an exact mapping. We note that a chiral decomposition based on perturbation calculation is proposed in recent works [18,72], which is distinct from our method.

## ACKNOWLEDGMENTS

This work was supported by the National Natural Science Foundation of China (Grants No. 12141401, No. 11874160, No. 22273029, and No. 11534001), the National Key Research and Development Program of China (Grants No. 2022YFA1403501 and No. 2017YFA040351), and the Fundamental Research Funds for the Central Universities (HUST: Grant No. 2017KFYXJJ027).

## APPENDIX A: DERIVATION OF THE MSD OF A GENERAL DTMLG

Here we derive the decoupled Hamiltonian in Eqs. (27) and (28). We start from the Hamiltonian of a general $(X+Y+Z)$-DTMLG with mirror symmetry as given in Eq. (17).

Considering the mirror symmetry, we use the parity-resolved basis, as given in Eq. (26). The corresponding unitary transformation is

$$U=\frac{1}{\sqrt{2}}\begin{pmatrix} E & 0 & \gamma \\ 0 & \sqrt{2}I & 0 \\ \gamma & 0 & -E \end{pmatrix}. \tag{A1}$$

Here $E$ is a $2(N-1)\times 2(N-1)$ identity matrix, and $\gamma$ is a $2(N-1)\times 2(N-1)$ matrix as

$$\gamma=\begin{pmatrix} 0 & \cdots & I \\ \vdots & I & \vdots \\ I & \cdots & 0 \end{pmatrix}. \tag{A2}$$

So the general Hamiltonian after this unitary transformation is

$$H_{\mathrm{mirr}}=U^{-1}H_0U=\frac{1}{2}\begin{pmatrix} H_{\mathrm{down}}+\gamma H_{\mathrm{up}}\gamma & \sqrt{2}(T_{dm}^\dagger+\gamma T_{um}) & H_{\mathrm{down}}\gamma-\gamma H_{\mathrm{up}} \\ \sqrt{2}(T_{dm}+T_{um}^\dagger\gamma) & 2H_N & \sqrt{2}(T_{dm}\gamma-T_{um}^\dagger) \\ \gamma H_{\mathrm{down}}-H_{\mathrm{up}}\gamma & \sqrt{2}(\gamma T_{dm}^\dagger-T_{um}) & \gamma H_{\mathrm{down}}\gamma+H_{\mathrm{up}} \end{pmatrix}. \tag{A3}$$

Now we need to use mirror symmetry, which implies

$$\begin{aligned} H_1 &= H_L \\ H_2 &= H_{L-1} \\ &\vdots \\ H_{N-1} &= H_{N+1} \\ T_{1,2} &= T^\dagger_{L-1,L} \\ T_{2,3} &= T^\dagger_{L-2,1} \\ &\vdots \\ T_{N-1,N} &= T^\dagger_{N,N+1}. \end{aligned} \tag{A4}$$

With the help of mirror symmetry, we also can verify $H_{\text{down}} = \gamma H_{\text{up}} \gamma$ and $T^\dagger_{dm} = \gamma T_{um}$. From Eq. (A3), we finally get

$$H_{\text{mirr}} = \begin{pmatrix} H_{\text{down}} & \sqrt{2}T^\dagger_{dm} & 0 \\ \sqrt{2}T_{dm} & H_N & 0 \\ 0 & 0 & H_{\text{up}} \end{pmatrix}, \tag{A5}$$

which is just Eq. (27) in the main text.

## APPENDIX B: DERIVATION OF THE $H_V$

Here we give a derivation of the influence of perpendicular electric field $E_\perp$ under parity-resolved basis, i.e., Eqs. (29) and (30) in the main text. With the original Bloch wave basis $\{|A_i\rangle, |B_i\rangle\}$, the Hamiltonian of $E_\perp$ is expressed as a block-diagonal matrix

$$H_0^V = VI \otimes \begin{pmatrix} N-1 & & & & & \\ & N-2 & & & & \\ & & \ddots & & & \\ & & & 0 & & \\ & & & & \ddots & \\ & & & & & -(N-2) \\ & & & & & & -(N-1) \end{pmatrix}, \tag{B1}$$

where $V$ is the potential difference between adjacent layers. For convenience, we define a new block-diagonal matrix

$$\chi = I \otimes \begin{pmatrix} N-1 & & & & \\ & N-2 & & & \\ & & \cdots & & \\ & & & 2 & \\ & & & & 1 \end{pmatrix}, \tag{B2}$$

and then

$$H_0^V = V \begin{pmatrix} \chi & 0 & 0 \\ 0 & 0 & 0 \\ 0 & 0 & -\gamma\chi\gamma \end{pmatrix}. \tag{B3}$$

Under the parity-resolved basis, we have

$$H_V = U^{-1} H_0^V U = V \begin{pmatrix} 0 & 0 & \chi\gamma \\ 0 & 0 & 0 \\ \gamma\chi & 0 & 0 \end{pmatrix}, \tag{B4}$$

where the unitary matrix is given by Eq. (A1). We then define $\Delta = V\chi\gamma$, and finally we get

$$H_V = \begin{pmatrix} 0 & D \\ D^\dagger & 0 \end{pmatrix}, \tag{B5}$$

where D is given in Eq. (30) of the main text.

## APPENDIX C: MSD OF THE DTMLG BASED ON A-A STACKING

### 1. MSD of the (A-AA-A)-DTMLG

Here we give the MSD of the (A-AA-A)-DTMLG. The Hamiltonian of the (A-AA-A)-DTMLG based on Eq. (1) under basis $\{|A_i\rangle, |B_i\rangle\}$ $(i = 1, 2, 3, 4)$ is

$$H_0 = \begin{pmatrix} H_1 & \widetilde{T}^\dagger_{1,2} & 0 & 0 \\ \widetilde{T}_{1,2} & H_2 & \overline{T}^\dagger_{2,3} & 0 \\ 0 & \overline{T}_{2,3} & H_3 & \widetilde{T}^\dagger_{3,4} \\ 0 & 0 & \widetilde{T}_{3,4} & H_4 \end{pmatrix}, \tag{C1}$$

where the interlayer hopping between AA-stacked graphene is denoted by

$$\overline{T}_{23} = \begin{pmatrix} t_\perp & 0 \\ 0 & t_\perp \end{pmatrix}. \tag{C2}$$

The mirror symmetry in this system implies that

$$\begin{aligned} H_1 &= H_4, \\ H_2 &= H_3, \\ \widetilde{T}_{1,2} &= \widetilde{T}^\dagger_{3,4}, \end{aligned} \tag{C3}$$

according to mirror symmetry, we can define a set of parity-resolved bases similar to Eq. (7), and the corresponding unitary transformation is

$$U = \frac{1}{\sqrt{2}} \begin{pmatrix} I & 0 & 0 & I \\ 0 & I & I & 0 \\ 0 & I & -I & 0 \\ I & 0 & 0 & -I \end{pmatrix}. \tag{C4}$$

The final result under this basis transformation is

$$\begin{aligned} H_{\text{mirr}} &= U^{-1} H_0 U \\ &= \begin{pmatrix} H_1 & \widetilde{T}^\dagger_{12} & 0 & 0 \\ \widetilde{T}_{12} & H_2 + \overline{T}_{23} & 0 & 0 \\ 0 & 0 & H_2 - \overline{T}_{23} & \widetilde{T}_{12} \\ 0 & 0 & \widetilde{T}^\dagger_{12} & H_1 \end{pmatrix}. \end{aligned} \tag{C5}$$

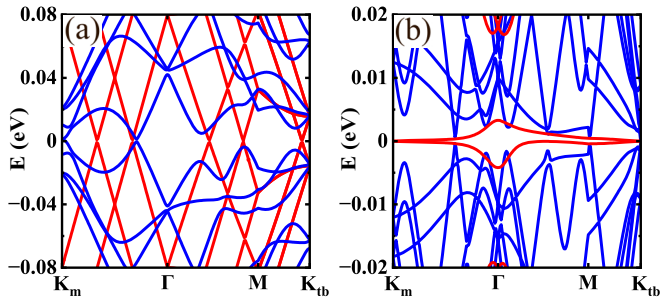


FIG. 7. (a) The band structure of AA + A + AA structure at 1.54° and (b) is of A + AAA + A at 1.05°.The blue solid line belongs to $H_{\mathrm{A+AA}}$ ($H'_{\mathrm{A+AA}}$) and the red solid line belongs to $H_{\mathrm{AA}}$ ($H_{\mathrm{TBG}}$) corresponding to (a) [(b)]. For AA + A + AA systems the two flat bands of BA + A + AB have been destroyed, and in A + AAA + A systems the four flat bands of A + ABA + A become two, which come from $H_{\mathrm{TBG}}$ according to the parity-resolved Hamiltonian.

In principle, A-AA-A double-twisted tetralayer graphene is decoupled into two subsystems. One (even parity) is TBG with an additional $\overline{T}_{23}$ term, which should be viewed as an equivalent onsite potential. The other (odd parity) is the same, but the onsite potential term now becomes $-\overline{T}_{23}$.

### 2. MSD of the (AA + A + AA)-stacked graphene system

Here we give the mirror MSD of the (AA + A + AA)-stacked graphene system. In the (2 + 1 + 2)-DTMLG, if the Bernal stacking is changed to AA stacking, we will get (AA + A + AA)-stacked graphene system. The total Hamiltonian can be decoupled in the same way:

$$H_{\mathrm{mirr}} = \begin{pmatrix} H_{\mathrm{A+AA}} & 0 \\ 0 & H_{\mathrm{AA}} \end{pmatrix} = \begin{pmatrix} H_1 & \overline{T}^{\dagger}_{1,2} & 0 & 0 & 0 \\ \overline{T}_{1,2} & H_2 & \sqrt{2}\widetilde{T}^{\dagger}_{2,3} & 0 & 0 \\ 0 & \sqrt{2}\widetilde{T}_{2,3} & H_3 & 0 & 0 \\ 0 & 0 & 0 & H_2 & \overline{T}_{1,2} \\ 0 & 0 & 0 & \overline{T}^{\dagger}_{1,2} & H_1 \end{pmatrix}, \quad \text{(C6)}$$

where the interlayer hopping between layer 1 (5) and layer 2 (4) is

$$\overline{T}_{12} = \begin{pmatrix} t_{\perp} & 0 \\ 0 & t_{\perp} \end{pmatrix}. \quad \text{(C7)}$$

Here, $H_{\mathrm{A+AA}}$ denotes a twisted trilayer system, which is composed of an AA-stacked bilayer and an SLG. An additional $\sqrt{2}$ factor appears at the moiré interlayer hopping terms. Meanwhile, $H_{\mathrm{AA}}$ represents AA-stacked bilayer graphene.

The band structures of such (AA + A + AA)-stacked graphene system are shown in Fig. 7(a) at 1.54°, where the blue (red) lines represent the bands of $H_{\mathrm{A+AA}}$ ($H_{\mathrm{AA}}$). Note that there is no flat band in this system.

### 3. MSD of the (A + AAA + A)-stacked graphene system

With MSD, the decoupled Hamiltonian of the (A + AAA + A)-stacked graphene system is

$$H_{\mathrm{mirr}} = \begin{pmatrix} H'_{\mathrm{A+AA}} & 0 \\ 0 & H_{\mathrm{TBG}} \end{pmatrix} = \begin{pmatrix} H_1 & \widetilde{T}^{\dagger}_{1,2} & 0 & 0 & 0 \\ \widetilde{T}_{1,2} & H_2 & \sqrt{2}\overline{T}^{\dagger}_{2,3} & 0 & 0 \\ 0 & \sqrt{2}\overline{T}_{2,3} & H_3 & 0 & 0 \\ 0 & 0 & 0 & H_2 & \widetilde{T}_{1,2} \\ 0 & 0 & 0 & \widetilde{T}^{\dagger}_{1,2} & H_1 \end{pmatrix}. \quad \text{(C8)}$$

In this case, the interlayer hopping between layers 2 and 3 is

$$\overline{T}_{23} = \begin{pmatrix} t_{\perp} & 0 \\ 0 & t_{\perp} \end{pmatrix}. \quad \text{(C9)}$$

Here $H'_{\mathrm{A+AA}}$ also denotes a twisted trilayer system, which consists of an AA-stacked bilayer graphene and an SLG. Now, the $\sqrt{2}$ factor is associated with $\overline{T}_{23}$. $H_{\mathrm{TBG}}$ represents twisted bilayer graphene.

The band structures of this (A + AAA + A)-stacked graphene system are shown in Fig. 7(b) at 1.05°, where the blue (red) lines represent the bands of $H'_{\mathrm{A+AA}}$ ($H_{\mathrm{TBG}}$). In this case, we get two flat bands resulting from $H_{\mathrm{TBG}}$.


[1] Y. Cao, V. Fatemi, S. Fang, K. Watanabe, T. Taniguchi, E. Kaxiras, and P. Jarillo-Herrero, Nature (London) **556**, 43 (2018).

[2] Y. Cao, V. Fatemi, A. Demir, S. Fang, S. L. Tomarken, J. Y. Luo, J. D. Sanchez-Yamagishi, K. Watanabe, T. Taniguchi, E. Kaxiras *et al.*, Nature (London) **556**, 80 (2018).

[3] X. Lu, P. Stepanov, W. Yang, M. Xie, M. A. Aamir, I. Das, C. Urgell, K. Watanabe, T. Taniguchi, G. Zhang *et al.*, Nature (London) **574**, 653 (2019).

[4] Y. Cao, D. Rodan-Legrain, J. M. Park, N. F. Yuan, K. Watanabe, T. Taniguchi, R. M. Fernandes, L. Fu, and P. Jarillo-Herrero, Science **372**, 264 (2021).

[5] T. J. Peltonen, R. Ojajärvi, and T. T. Heikkilä, Phys. Rev. B **98**, 220504(R) (2018).

[6] F. Wu, A. H. MacDonald, and I. Martin, Phys. Rev. Lett. **121**, 257001 (2018).

[7] W. Qin, B. Zou, and A. H. MacDonald, Phys. Rev. B **107**, 024509 (2023).

[8] Z. Ma, S. Li, Y.-W. Zheng, M.-M. Xiao, H. Jiang, J.-H. Gao, and X. Xie, Sci. Bull. **66**, 18 (2021).

[9] J. Liu, Z. Ma, J. Gao, and X. Dai, Phys. Rev. X **9**, 031021 (2019).

[10] S. Zhang, X. Dai, and J. Liu, Phys. Rev. Lett. **128**, 026403 (2022).

[11] Y. Park, B. L. Chittari, and J. Jung, Phys. Rev. B **102**, 035411 (2020).

[12] L. Rademaker, I. V. Protopopov, and D. A. Abanin, Phys. Rev. Res. **2**, 033150 (2020).

[13] M. Koshino, Phys. Rev. B **99**, 235406 (2019).
[14] P. J. Ledwith, A. Vishwanath, and E. Khalaf, Phys. Rev. Lett. **128**, 176404 (2022).
[15] J. Dong, P. J. Ledwith, E. Khalaf, J. Y. Lee, and A. Vishwanath, Exact many-body ground states from decomposition of ideal higher chern bands: Applications to chirally twisted graphene multilayers, Phys. Rev. Res. **5**, 023166 (2023).
[16] X. Lin, H. Zhu, and J. Ni, Phys. Rev. B **104**, 125421 (2021).
[17] F. Haddadi, Q. Wu, A. J. Kruchkov, and O. V. Yazyev, Nano Lett. **20**, 2410 (2020).
[18] S. Zhang, B. Xie, Q. Wu, J. Liu, and O. V. Yazyev, Nano Lett., **23**, 2921 (2023).
[19] J. Y. Lee, E. Khalaf, S. Liu, X. Liu, Z. Hao, P. Kim, and A. Vishwanath, Nat. Commun. **10**, 5333 (2019).
[20] S.-Y. Li, Y. Zhang, Y.-N. Ren, J. Liu, X. Dai, and L. He, Phys. Rev. B **102**, 121406(R) (2020).
[21] J. Liu and X. Dai, Nat. Rev. Phys. **3**, 367 (2021).
[22] H. Polshyn, J. Zhu, M. A. Kumar, Y. Zhang, F. Yang, C. L. Tschirhart, M. Serlin, K. Watanabe, T. Taniguchi, A. H. MacDonald *et al.*, Nature (London) **588**, 66 (2020).
[23] J. M. Park, Y. Cao, K. Watanabe, T. Taniguchi, and P. Jarillo-Herrero, Nature (London) **590**, 249 (2021).
[24] Z. Hao, A. M. Zimmerman, P. Ledwith, E. Khalaf, D. H. Najafabadi, K. Watanabe, T. Taniguchi, A. Vishwanath, and P. Kim, Science **371**, 1133 (2021).
[25] Y. Cao, J. M. Park, K. Watanabe, T. Taniguchi, and P. Jarillo-Herrero, Nature (London) **595**, 526 (2021).
[26] H. Kim, Y. Choi, C. Lewandowski, A. Thomson, Y. Zhang, R. Polski, K. Watanabe, T. Taniguchi, J. Alicea, and S. Nadj-Perge, Nature (London) **606**, 494 (2022).
[27] X. Liu, N. J. Zhang, K. Watanabe, T. Taniguchi, and J. I. A. Li, Nat. Phys. **18**, 522 (2022).
[28] S. Turkel, J. Swann, Z. Zhu, M. Christos, K. Watanabe, T. Taniguchi, S. Sachdev, M. Scheurer, E. Kaxiras, C. Dean, and A. Pasupathy, Science **376**, 193 (2022).
[29] E. Khalaf, A. J. Kruchkov, G. Tarnopolsky, and A. Vishwanath, Phys. Rev. B **100**, 085109 (2019).
[30] S. Carr, C. Li, Z. Zhu, E. Kaxiras, S. Sachdev, and A. Kruchkov, Nano Lett. **20**, 3030 (2020).
[31] X. Li, F. Wu, and A. H. MacDonald, arXiv:1907.12338.
[32] C. Lei, L. Linhart, W. Qin, F. Libisch, and A. H. MacDonald, Phys. Rev. B **104**, 035139 (2021).
[33] Z. Wu, Z. Zhan, and S. Yuan, Sci. China Phys. Mech. Astron. **64**, 267811 (2021).
[34] P. J. Ledwith, E. Khalaf, Z. Zhu, S. Carr, E. Kaxiras, and A. Vishwanath, arXiv:2111.11060.
[35] J. Shin, B. L. Chittari, and J. Jung, Phys. Rev. B **104**, 045413 (2021).
[36] D. Călugăru, F. Xie, Z.-D. Song, B. Lian, N. Regnault, and B. A. Bernevig, Phys. Rev. B **103**, 195411 (2021).
[37] F. Xie, N. Regnault, D. Călugăru, B. A. Bernevig, and B. Lian, Phys. Rev. B **104**, 115167 (2021).
[38] A. Ramires and J. L. Lado, Phys. Rev. Lett. **127**, 026401 (2021).
[39] M. Christos, S. Sachdev, and M. S. Scheurer, Phys. Rev. X **12**, 021018 (2022).
[40] X. Lin, C. Li, K. Su, and J. Ni, Phys. Rev. B **106**, 075423 (2022).
[41] E. Lake and T. Senthil, Phys. Rev. B **104**, 174505 (2021).
[42] Y.-Z. Chou, F. Wu, J. D. Sau, and S. Das Sarma, Phys. Rev. Lett. **127**, 217001 (2021).
[43] W. Qin and A. H. MacDonald, Phys. Rev. Lett. **127**, 097001 (2021).
[44] V. o. T. Phong, P. A. Pantaleón, T. Cea, and F. Guinea, Phys. Rev. B **104**, L121116 (2021).
[45] I. A. Assi, J. P. F. LeBlanc, M. Rodriguez-Vega, H. Bahlouli, and M. Vogl, Phys. Rev. B **104**, 195429 (2021).
[46] H. Scammell, J. Li, and M. Scheurer, 2D Mater. **9**, 025027 (2022).
[47] R. Samajdar, Y. Teng, and M. S. Scheurer, Phys. Rev. B **106**, L201403 (2022).
[48] D. Guerci, P. Simon, and C. Mora, Phys. Rev. Res. **4**, L012013 (2022).
[49] Y. Li, S. Zhang, F. Chen, L. Wei, Z. Zhang, H. Xiao, H. Gao, M. Chen, S. Liang, D. Pei, L. Xu, K. Watanabe, T. Taniguchi, L. Yang, F. Miao, J. Liu, B. Cheng, M. Wang, Y. Chen, and Z. Liu, Adv. Mater. **34**, 2205996 (2022).
[50] A. Fischer, Z. Goodwin, A. Mostofi, J. Lischner, D. Kennes, and L. Klebl, npj Quantum Mater. **7**, 5 (2022).
[51] Y. Cao, D. Chowdhury, D. Rodan-Legrain, O. Rubies-Bigorda, K. Watanabe, T. Taniguchi, T. Senthil, and P. Jarillo-Herrero, Phys. Rev. Lett. **124**, 076801 (2020).
[52] E. Y. Andrei and A. H. MacDonald, Nat. Mater. **19**, 1265 (2020).
[53] H. Polshyn, M. Yankowitz, S. Chen, Y. Zhang, K. Watanabe, T. Taniguchi, C. R. Dean, and A. F. Young, Nat. Phys. **15**, 1011 (2019).
[54] S. Lisi, X. Lu, T. Benschop, T. A. de Jong, P. Stepanov, J. R. Duran, F. Margot, I. Cucchi, E. Cappelli, A. Hunter *et al.*, Nat. Phys. **17**, 189 (2021).
[55] Y. Choi, J. Kemmer, Y. Peng, A. Thomson, H. Arora, R. Polski, Y. Zhang, H. Ren, J. Alicea, G. Refael *et al.*, Nat. Phys. **15**, 1174 (2019).
[56] A. L. Sharpe, E. J. Fox, A. W. Barnard, J. Finney, K. Watanabe, T. Taniguchi, M. Kastner, and D. Goldhaber-Gordon, Science **365**, 605 (2019).
[57] N. P. Kazmierczak, M. Van Winkle, C. Ophus, K. C. Bustillo, S. Carr, H. G. Brown, J. Ciston, T. Taniguchi, K. Watanabe, and D. K. Bediako, Nat. Mater. **20**, 956 (2021).
[58] Y. Saito, F. Yang, J. Ge, X. Liu, T. Taniguchi, K. Watanabe, J. Li, E. Berg, and A. F. Young, Nature (London) **592**, 220 (2021).
[59] D. Wong, K. P. Nuckolls, M. Oh, B. Lian, Y. Xie, S. Jeon, K. Watanabe, T. Taniguchi, B. A. Bernevig, and A. Yazdani, Nature (London) **582**, 198 (2020).
[60] M. Oh, K. P. Nuckolls, D. Wong, R. L. Lee, X. Liu, K. Watanabe, T. Taniguchi, and A. Yazdani, Nature (London) **600**, 240 (2021).
[61] H. Yoo, R. Engelke, S. Carr, S. Fang, K. Zhang, P. Cazeaux, S. H. Sung, R. Hovden, A. W. Tsen, T. Taniguchi *et al.*, Nat. Mater. **18**, 448 (2019).
[62] A. C. Gadelha, D. A. Ohlberg, C. Rabelo, E. G. Neto, T. L. Vasconcelos, J. L. Campos, J. S. Lemos, V. Ornelas, D. Miranda, R. Nadas *et al.*, Nature (London) **590**, 405 (2021).
[63] Y. Jiang, X. Lai, K. Watanabe, T. Taniguchi, K. Haule, J. Mao, and E. Y. Andrei, Nature (London) **573**, 91 (2019).
[64] Y. Xie, B. Lian, B. Jäck, X. Liu, C.-L. Chiu, K. Watanabe, T. Taniguchi, B. A. Bernevig, and A. Yazdani, Nature (London) **572**, 101 (2019).

[65] X. Liu, Z. Wang, K. Watanabe, T. Taniguchi, O. Vafek, and J. Li, Science **371**, 1261 (2021).

[66] J. M. Park, Y. Cao, L.-Q. Xia, S. Sun, K. Watanabe, T. Taniguchi, and P. Jarillo-Herrero, Nat. Mater. **21**, 877 (2022).

[67] G. Burg, E. Khalaf, Y. Wang, K. Watanabe, T. Taniguchi, and E. Tutuc, Nat. Mater. **21**, 884 (2022).

[68] Z. Liu, W. Shi, T. Yang, and Z. Zhang, J. Mater. Sci. Technol. **111**, 28 (2022).

[69] N. Leconte, Y. Park, J. An, A. Samudrala, and J. Jung, 2D Mater. **9**, 044002 (2022).

[70] M. Liang, M.-M. Xiao, Z. Ma, and J.-H. Gao, Phys. Rev. B **105**, 195422 (2022).

[71] Z. Ma, S. Li, M. Lu, D.-H. Xu, J.-H. Gao, and X. Xie, Sci. China Phys. Mech. Astron. **66**, 227211 (2023).

[72] B. Xie, R. Peng, S. Zhang, and J. Liu, npj Comput. Mater. **8**, 110 (2022).

[73] J. Shin, B. L. Chittari, Y. Jang, H. Min, and J. Jung, Phys. Rev. B **105**, 245124 (2022).

[74] C. Mora, N. Regnault, and B. A. Bernevig, Phys. Rev. Lett. **123**, 026402 (2019).

[75] X. Zhang, K.-T. Tsai, Z. Zhu, W. Ren, Y. Luo, S. Carr, M. Luskin, E. Kaxiras, and K. Wang, Phys. Rev. Lett. **127**, 166802 (2021).

[76] Z. Zhu, S. Carr, D. Massatt, M. Luskin, and E. Kaxiras, Phys. Rev. Lett. **125**, 116404 (2020).

[77] R. Bistritzer and A. H. MacDonald, Proc. Natl. Acad. Sci. USA **108**, 12233 (2011).

[78] P. Moon and M. Koshino, Phys. Rev. B **87**, 205404 (2013).

[79] M. Koshino, New J. Phys. **17**, 015014 (2015).

[80] M. Koshino and P. Moon, J. Phys. Soc. Jpn. **84**, 121001 (2015).

[81] Z. Ma, S. Li, M.-M. Xiao, Y.-W. Zheng, M. Lu, H. Liu, J.-H. Gao, and X. C. Xie, Front. Phys. **18**, 13307 (2023).

[82] M. Koshino and E. McCann, Phys. Rev. B **79**, 125443 (2009).

[83] P. Stepanov, Y. Barlas, S. Che, K. Myhro, G. Voigt, Z. Pi, K. Watanabe, T. Taniguchi, D. Smirnov, F. Zhang, R. K. Lake, A. H. MacDonald, and C. N. Lau, Proc. Natl. Acad. Sci. USA **116**, 10286 (2019).

[84] S. Chen, M. He, Y.-H. Zhang, V. Hsieh, Z. Fei, K. Watanabe, T. Taniguchi, D. H. Cobden, X. Xu, C. R. Dean *et al.*, Nat. Phys. **17**, 374 (2021).

[85] S. Xu, M. M. Al Ezzi, N. Balakrishnan, A. Garcia-Ruiz, B. Tsim, C. Mullan, J. Barrier, N. Xin, B. A. Piot, T. Taniguchi *et al.*, Nat. Phys. **17**, 619 (2021).

[86] M. He, Y.-H. Zhang, Y. Li, Z. Fei, K. Watanabe, T. Taniguchi, X. Xu, and M. Yankowitz, Nat. Commun. **12**, 4727 (2021).

[87] L.-H. Tong, Q. Tong, L.-Z. Yang, Y.-Y. Zhou, Q. Wu, Y. Tian, L. Zhang, L. Zhang, Z. Qin, and L.-J. Yin, Phys. Rev. Lett. **128**, 126401 (2022).

[88] J. Cao, M. Wang, S.-F. Qian, C.-C. Liu, and Y. Yao, Phys. Rev. B **104**, L081403 (2021).

[89] Y. Cao, D. Rodan-Legrain, O. Rubies-Bigorda, J. M. Park, K. Watanabe, T. Taniguchi, and P. Jarillo-Herrero, Nature (London) **583**, 215 (2020).

[90] X. Liu, Z. Hao, E. Khalaf, J. Lee, Y. Ronen, H. Yoo, D. Najafabadi, K. Watanabe, T. Taniguchi, A. Vishwanath, and P. Kim, Nature (London) **583**, 221 (2020).

[91] C. Shen, Y. Chu, Q. Wu, N. Li, S. Wang, Y. Zhao, J. Tang, J. Liu, J. Tian, K. Watanabe, T. Taniguchi, R. Yang, Z. Y. Meng, D. Shi, O. V. Yazyev, and G. Zhang, Nat. Phys. **16**, 520 (2020).

[92] R. Samajdar, M. S. Scheurer, S. Turkel, C. Rubio-Verdú, A. N. Pasupathy, J. W. F. Venderbos, and R. M. Fernandes, 2D Mater. **8**, 034005 (2021).

[93] H. Zhou, L. Holleis, Y. Saito, L. Cohen, W. Huynh, C. Patterson, F. Yang, T. Taniguchi, K. Watanabe, and A. Young, Science **375**, 774 (2022).

[94] S. C. de la Barrera, S. Aronson, Z. Zheng, K. Watanabe, T. Taniguchi, Q. Ma, P. Jarillo-Herrero, and R. Ashoori, Nat. Phys. **18**, 771 (2022).

[95] A. Seiler, F. Geisenhof, F. Winterer, K. Watanabe, T. Taniguchi, T. Xu, F. Zhang, and R. Weitz, Nature (London) **608**, 298 (2022).

[96] Z. A. H. Goodwin, V. Vitale, X. Liang, A. A. Mostofi, and J. Lischner, Electron. Struct. **2**, 034001 (2020).

[97] F. Guinea and N. R. Walet, Proc. Natl. Acad. Sci. USA **115**, 13174 (2018).

[98] M. J. Calderón and E. Bascones, Phys. Rev. B **102**, 155149 (2020).

[99] T. Cea, P. A. Pantaleón, N. R. Walet, and F. Guinea, Nano. Mater. Sci. **4**, 27 (2022).

[100] T. Cea, N. R. Walet, and F. Guinea, Phys. Rev. B **100**, 205113 (2019).

[101] C. T. S. Cheung, Z. A. H. Goodwin, V. Vitale, J. Lischner, and A. A. Mostofi, Electron. Struct. **4**, 025001 (2022).

[102] P. A. Pantaleón, T. Cea, R. Brown, N. R. Walet, and F. Guinea, 2D Mater. **8**, 044006 (2021).

[103] Z. A. H. Goodwin, L. Klebl, V. Vitale, X. Liang, V. Gogtay, X. van Gorp, D. M. Kennes, A. A. Mostofi, and J. Lischner, Phys. Rev. Mater. **5**, 084008 (2021).

[104] D. Ding, R. Niu, X. Han, Z. Qu, Z. Wang, Z. Li, Q. Liu, C. Han, and J. Lu, Chin. Phys. B **32**, 067204 (2023).

[105] Y. W. Choi and H. J. Choi, Phys. Rev. Lett. **127**, 167001 (2021).

[106] N. R. Finney, M. Yankowitz, L. Muraleetharan, K. Watanabe, T. Taniguchi, C. R. Dean, and J. C. Hone, Nat. Nanotechnol. **14**, 1029 (2019).

[107] M. Anđelković, S. P. Milovanović, L. Covaci, and F. M. Peeters, Nano Lett. **20**, 979 (2020).

[108] Z. Wang, Y. B. Wang, J. Yin, E. Tovari, Y. Yang, L. Lin, M. Holwill, J. Birkbeck, D. Perello, S. Xu *et al.*, Sci. Adv. **5**, eaay8897 (2019).

[109] Y. Chen, W.-T. Guo, Z.-S. Chen, S. Wang, and J.-M. Zhang, J. Phys.: Condens. Matter **34**, 125504 (2022).

[110] H. Oka and M. Koshino, Phys. Rev. B **104**, 035306 (2021).